Original Article

# Effect of sintering temperature on phase evolution, microstructure, and mechanical properties of La$_2$Ce$_2$O$_7$/40 wt.% YSZ composite ceramics

Ivana Parchovianská [a,*], Milan Parchoviansky [a], Aleksandra Nowicka [a], Anna Prnová [b], Peter Švančárek [b], Amirhossein Pakseresht [a]

[a] Centre for Functional and Surface Functionalized Glass, Alexander Dubček University of Trenčín, 911 50 Trenčín, Slovakia
[b] Joint Glass Centre of the IIC SAS, TnUAD, FChPT STU, Študentská 2, 911 50 Trenčín, Slovakia

## ARTICLE INFO

## ABSTRACT

In this work, La$_2$Ce$_2$O$_7$/40 wt% YSZ (LC40Z) mixed powders were used to fabricate composite bulk ceramics with their potential use as a material for high-performance thermal barrier coatings (TBCs). For this purpose, the effect of sintering temperature on the chemical reactivity of LC and YSZ was investigated via hot-pressing at the temperatures of 1300, 1400 and 1500 °C. X-ray diffraction analysis (XRD), Raman spectroscopy, and scanning electron microscopy (SEM) were utilized to characterize the phase and microstructure evolution in both LC40Z powder mixtures and composite bulk ceramics. Results showed that solid-solution reactions occurred between the YSZ and LC during hot-pressing of the LC40Z powder mixtures, indicated by a new phase of La$_2$Ce$_{0.2}$Zr$_{1.8}$O$_7$ (LCZ) observed in the XRD patterns. The detailed analysis of Raman spectra confirmed the gradual transition from fluorite LC to pyrochlore LCZ structure, which was demonstrated by the appearance of characteristic pyrochlore bands. All composites densified by hot-pressing exhibited a high relative density above 95%. The average grain size of the LC40Z composites increased significantly with increasing sintering temperature, while gradual pore-healing was observed. The associated mechanical properties of LC40Z ceramics were also reported. The Vickers hardness values increased with increasing sintering temperature, which is consistent with the microstructure evolution and relative density variations. The highest hardness, with a value of 10.99 ± 0.23 GPa, was achieved for the composite hot-pressed at 1500 °C. The fracture toughness results showed the same dependence on sintering temperature. The fracture toughness increased from 1.97 ± 0.15 to 2.4 ± 0.14 MPa m$^{1/2}$, indicating that the mechanical properties of the LC40Z composites can be tailored by changing the sintering temperature during hot-pressing.

# 1. Introduction

Thermal barrier coatings (TBCs) are widely used in modern gas turbines or aircraft engines to protect hot-section metallic components from excessive heat and combustion environments [1]. Currently, 8 wt% yttria-stabilized zirconia (YSZ) is the most commonly used top coat material in TBCs due to its high melting point (2680 °C), low thermal conductivity (2.1 W/m·K), and high thermal expansion coefficient (CTE) ($10.7 \cdot 10^{-6}$ $K^{-1}$) [2—6]. However, phase transformations and severe sintering occur during long-term operation at temperatures above 1200 °C, leading to premature spallation and failure of TBCs [7—10]. For this reason, alternative materials with high phase stability and low thermal conductivity are required for the development of next-generation TBCs operating at elevated temperatures.

In the last few years, rare-earth element-based ceramics have been at the center of interest as a potential material for TBCs due to their outstanding chemical and physical properties. The chemical formula of this type of ceramics can be indicated as $A_2B_2O_7$, where A represents $3^+$ cation (rare earth elements) and B shows a $4^+$ cation (Zr, Ce, Hf, Ti, etc.) [11]. These ternary oxides crystallize into an ordered pyrochlore-type structure (cubic, *Fd3m*) or a disordered fluorite-type structure (cubic, *Fm3m*), depending on the radii of A- and B-site cations [12]. The cubic pyrochlore structure is stable for the cation radii of $1.46 \leq r_A/r_B \leq 1.78$, whereas the defect fluorite structure is formed when $r_A/r_B$ is lower than 1.46 [13]. Among these complex oxides, $La_2Ce_2O_7$ (LC) is one of the most promising TBC materials for high-temperature applications, due to its high phase stability, and ability to withstand high temperatures (>1250 °C) [14,15]. Moreover, LC exhibits a higher CTE, lower heat transfer, and better calcium-magnesium-aluminum-silicate (CMAS) corrosion resistance than YSZ [14,16—18]. Different methods, such as solid-state synthesis [13,19], co-precipitation route [20,21], hydrothermal method [22,23], sol-gel [12,24], or molten salt method [25] can be employed for the synthesis of LC particles with various morphologies and crystallite sizes. The conventional solid-state synthesis is an easy and effective method to prepare nanosized LC with good powder homogeneity that is necessary for fabricating high-performance TBCs.

There are several studies about LC as an advanced candidate material for TBCs and a great effort has been made to improve the performance of LC TBCs. For instance, a published research work by Zhao et al. [26] discussed the influence of powder characteristics on the LC coating microstructures. Wang et al. [27] devoted their research to improving the thermal shock resistance and mechanical properties of LC TBC with segmented structure produced by plasma spraying. In the published report of Gao et al. [16], the microstructure evolution, mechanical properties, and thermal interaction of the plasma-sprayed LC TBC with CMAS were investigated, and the associated mechanism for LC TBC against CMAS penetration was also discussed. However, it has been reported, that LC exhibits poor mechanical properties, especially low fracture toughness, which leads to a short service life in the case of a single-layer LC TBC [28]. Moreover, the CTE of LC undergoes a dramatic decrease in the temperature range between 200 and 400 °C, causing the generation of high thermal stress, which is responsible for the failure of the ceramic coatings [14,17].

Several authors proposed the combination of LC and YSZ as a solution to overcome the shortcomings of single YSZ or LC TBCs. For example, Dehkharghani et al. [29] dedicated their work to improving the thermal shock resistance and fracture toughness of $La_2Ce_2O_7$/YSZ thermal barrier coatings. The best thermal shock resistance was achieved in LC-50 wt% YSZ composite coating, which was able to withstand 350 thermal cycles. The results also indicated that a higher fraction of YSZ enhanced the fracture toughness due to a higher energy-relieving rate. Ma et al. [30] developed a novel TBC system based on LC/8YSZ deposited by electron beam physical vapor deposition (EB-PVD). It was found that double-ceramic-layer systems have a longer lifespan compared to a single LC layer, and much longer than that of the 8YSZ single-layer system under a burner rig test. Zhang et al. [31] also reported improved mechanical performance, thermophysical properties and thermal shock resistance of YSZ-toughened LC composite TBCs.

The above-mentioned studies were mostly focused on investigating LC/YSZ composite coatings and there is little knowledge about the properties of LC/YSZ bulk ceramics. However, it is equally as important to understand the sintering behavior, phase stability, and microstructure evolution of dense LC/YSZ ceramics as to examine their mechanical and thermal properties. The first step for producing high performance TBCs is to find an optimized composition and structure with a high thermal insulation effect and low residual stress. In a previous work [32], the thermal behavior and mechanical properties of hot-pressed LC/YSZ composites with different content of YSZ were investigated, where the lowest thermal conductivity in the temperature range of 400—1000 °C was found for the bulk sample containing 40 wt% YSZ. Therefore, in the present study, the sintering behavior and chemical reactivity of LC and YSZ were investigated for LC/40 wt% YSZ (LC40Z) composite ceramics via hot-press experiments at different temperatures. The influence of phase transformation on the microstructure and mechanical properties was also analyzed, since the absence of systematic studies and reliable information can lead to inconsistent knowledge about the performance of TBC materials.

# 2. Experimental

## 2.1. Powder synthesis and bulk specimen preparation

The conventional method of powder homogenization was used to prepare a LC40Z composite powder mixture containing 40 wt% (56 mol.%) of YSZ (8 mol.% yttria-stabilized zirconia, Inframat, Manchester, CT, USA) and 60 wt% (44 mol.%) of LC powder. The starting LC powder with a cubic fluorite structure was synthesized via a solid-state reaction at 1400 °C.

The fabrication procedure of the LC powder is described in our previous work [33]. To obtain the final LC40Z powder composite, the calculated amounts of LC and YSZ powders were mixed and homogenized for 24 h with isopropanol and $ZrO_2$ milling balls. After mixing, the suspension was heated under constant stirring to remove the excess alcohol. The product was dried in an oven at 100 °C for 24 h, crushed, and sieved through a 100 μm mesh screen. To study the chemical reactivity between the LC and YSZ, the composite powder mixture was calcined at 1300, 1400, and 1500 °C for 6 h in an electric furnace.

The final disk-shaped composite bulk samples were prepared by sintering the LC40Z powder mixture via hot pressing (Clasic 0220 ZL, Clasic, Řevnice, The Czech Republic). The sintering was performed in a vacuum atmosphere at different temperatures, i.e. 1300, 1400, and 1500 °C, with a holding time of 1 h. A uniaxial load of 30 MPa was applied and maintained for all hot-press experiments. A BN layer was used as an interface to prevent direct contact between the sample and a graphite die.

## 2.2. Characterization techniques

A thermal behavior study of the LC40Z powder mixture was carried out using thermogravimetry and differential scanning calorimetry (TG/DSC, Netzsch STA 449 F3 Jupiter, NETZSCH-Gerätebau GmbH, Selb, Germany) in a nitrogen atmosphere. The TG-DSC experiments were performed in the temperature range of 25−1300 °C with a heating rate of 10 °C/min. A sample weight of ≈20 mg was used for the TG/DSC analysis.

Crystalline phases in both powder and bulk samples were identified by means of X-ray diffraction analysis (XRD) using a PANalytical Empyrean DY1098 diffractometer (Panalytical, BV, Almelo, The Netherlands). Spectra within the range of 20° and 80° over 2θ angles were recorded at 45 kV and 40 mA using Cu Kα radiation (λ = 1.5405 Å). Diffraction records were evaluated using HighScore Plus (v. 3.0.4, Panalytical, Almelo, The Netherlands) with the use of the PDF4 database. The lattice parameters were determined from XRD using the most intense (111) and (222) lines, according to Eq. (1):

$$d = \frac{a}{\sqrt{h^2 + k^2 + l^2}} \qquad (1)$$

where $a$ is the lattice parameter, (hkl) is Miller indices, and $d$ is interplanar spacing. Rietveld refinement of XRD data was used to calculate the relative contents of the crystalline phases in samples. The crystalline structure of the LC40Z powders and composite bulk samples was further determined by Raman spectroscopy on a RENISHAW inVia Reflex Raman spectrometer (RENISHAW, Wotton-under-Edge, England, UK), using an excitation wavelength of 532 nm. Raman spectra were recorded in the range of the Raman shift of 100−1000 $cm^{-1}$.

The bulk densities of the hot-pressed composites were measured using the Archimedes method by weighing in air and deionized water as an immersion medium. The theoretical densities of the bulk samples were estimated based on the mixing law using the theoretical densities of the constituents and their relative contents determined by Rietveld refinement. The relative densities were then expressed as the ratio of the bulk density of the composites to the theoretical density.
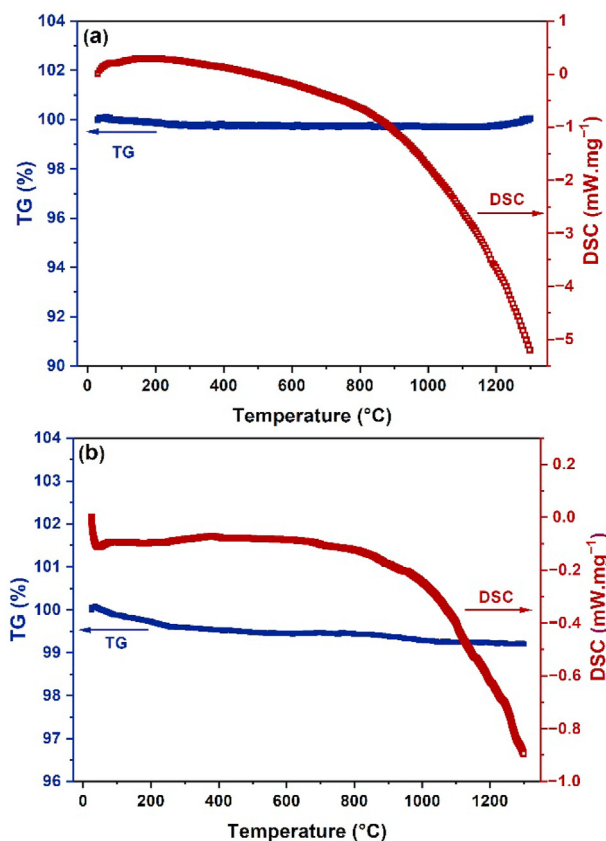


Fig. 1 − **TG and DSC curves of the prepared powders: (a) LC powder; (b) LC40Z powder mixture.**

Morphologies of the prepared powders and microstructures of the bulk samples after sintering were investigated by scanning electron microscopy (SEM, JEOL JSM 7600 F, JEOL, Tokyo, Japan). Energy-dispersive X-ray spectroscopy (EDXS, Oxford Instruments, Abingdon, UK) was employed to determine the element distribution in the bulk samples. The average grain size of bulk samples was determined by the linear intercept method from SEM micrographs using the software Lince (TU Darmstadt, Darmstadt, Germany). For this purpose, the polished cross-sections were thermally etched in a horizontal furnace (Clasic HT1600, Clasic, Řevnice, The Czech Republic) at 100 °C below sintering temperature for 1 h using a heating rate of 10 °C/min.

Mechanical properties, i.e. microhardness ($H_V$) and fracture toughness ($K_{IC}$), of the LC40Z bulk specimens were measured by Vickers' indentation (Micro Hardness Tester, WIKI 200, AFFRI, Wood Dale, IL, USA) with a 5 N load (0.5 kgf) applied for 10 s on embedded and polished samples. The $K_{IC}$ values were calculated from the length of the radial cracks of the Vickers indentations according to the equation proposed by Shetty [34], (2):

$$K_{IC} = 0,0889\sqrt{\frac{HV \cdot 1000 \cdot F}{4 \cdot L}} \qquad (2)$$

where $H_V$ is the Vickers hardness [GPa], F is the indentation load [N], and L = c-d where c is the length of the crack and d is the length of the diagonal. The average values of $H_V$ and $K_{IC}$ for each sample were obtained from 10 measurements.
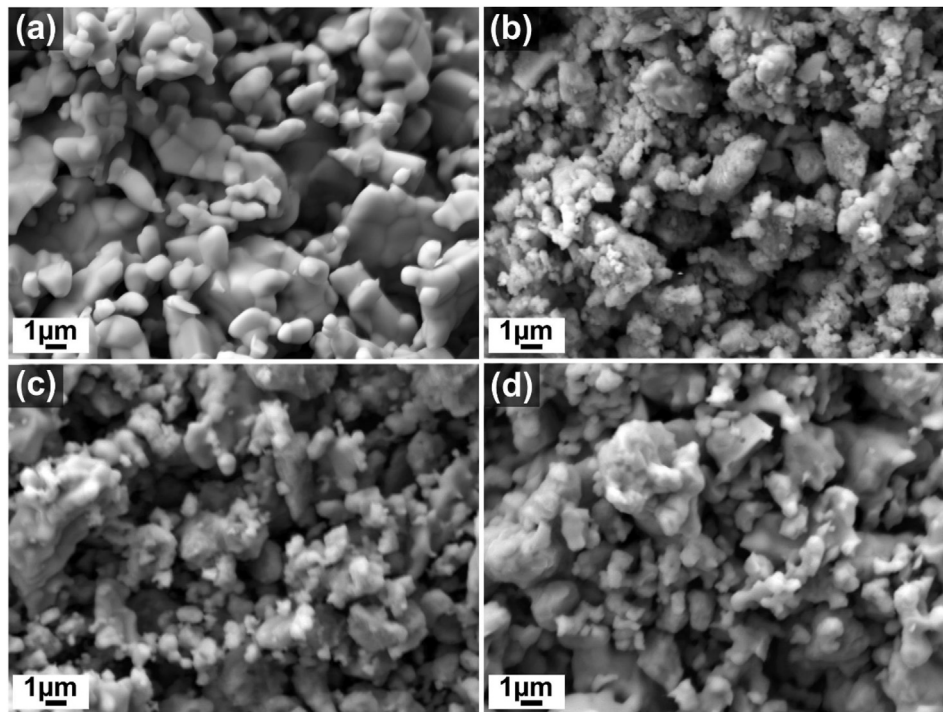
**Fig. 2 − SEM images of the prepared powders calcined at different temperatures for 6 h: (a) LC powder; (b) LC40Z 1300 °C; (c) LC40Z 1400 °C; (d) LC40Z 1500 °C.**

## 3. Results and discussion

### 3.1. Thermal behavior of the LC40Z powder mixture

To investigate the possible phase transformations in both LC powder and LC40Z powder mixture, TG/DSC records were measured from room temperature to 1300 °C, as shown in Fig. 1. For both samples, no thermal decomposition or phase transformations are observed in the DSC curves within the experimental temperatures. In the DSC curve of the LC40Z powder mixture (Fig. 1b), only an endothermic process with a peak temperature at ~70 °C is observed, and corresponds to a release of molecular water. In the case of the TG curves, no mass change is evident over the tested temperature range; less than ~0.8% of mass loss can be attributed to the evaporation of absorbed moisture. These results agree with a study by Ma et al. [30]. The authors reported good chemical compatibility of LC with YSZ powders since neither endothermic peak nor exothermic peak was observed during DSC measurement of LC/YSZ mixed powders in the temperature range of 200−1300 °C.

To investigate the high-temperature capability and chemical reactivity between the LC and YSZ during prolonged processing at elevated temperatures, the LC40Z composite powder mixtures were calcined at 1300, 1400, and 1500 °C for 6 h, as discussed in the following sections.

### 3.2. Morphology of the LC40Z powder mixtures

SEM was employed to obtain information about the morphology and size of the produced powders after heat treatment at different temperatures. Fig. 2a illustrates the SEM image of the as-prepared LC powder calcined at 1400 °C. It can be seen that LC particles are irregular in shape, while each particle is an aggregation consisting of small primary sintered nanoparticles with a size of up to 1 μm. This typical agglomerated morphology is similar to other studies in the literature. Wang et al. [25] observed that LC nano-powders produced by the molten salt method are agglomerated and composed of small particles with an average size between 50 nm and 80 nm. Joulia et al. [35] reported that the LC powder prepared by the citrate route consisted of fine and uniform 50−100 nm particles, but at 1400 °C the sintering effect resulted in a significant increase in grain size.

In the case of composite powder mixtures calcined up to 1500 °C (Fig. 2b−d), polydispersing nature of the powders was observed. It is also visible that large particle blocks are aggregates of small particles, most of them smaller than 1 μm. An increase in the calcining temperature up to 1500 °C at a given holding time of 6 h showed no considerable changes in the powder morphology and particle sizes.

### 3.3. Phase composition analysis of the LC40Z powder mixtures and hot-pressed composites

The chemical reactivity between LC and YSZ and phase evolution in LC40Z powder mixtures and hot-pressed bulk samples were investigated by XRD, as shown in Figs. 3 and 4, respectively. The XRD profile for the as-synthesized LC powder without YSZ addition is also displayed in Fig. 3 for comparison. The resulting diffraction pattern of the LC powder shows only one phase after synthesis, which closely matches the cubic fluorite phase of $CeO_2$ [19,36]. No additional peaks
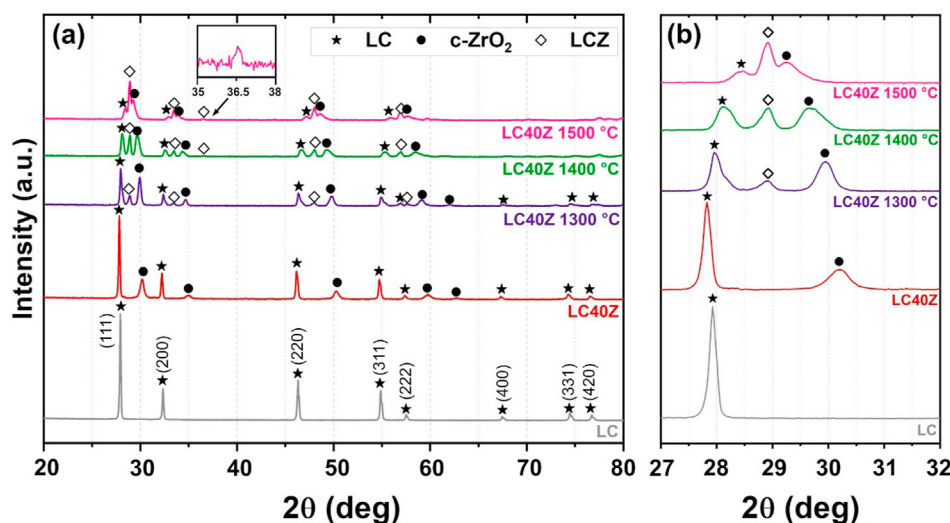
**Fig. 3 – XRD patterns of the LC powder and LC40Z powder mixtures calcined at different temperatures for 6 h: (a) 2θ range 20−80° (insert in XRD pattern shows a magnification of the LCZ pyrochlore peak at 2θ = 36.5°); (b) 2θ range 27−32°.**

corresponding to unreacted reagents, i.e. $La_2O_3$ or $CeO_2$, were found in the XRD record, confirming the formation of $La_2Ce_2O_7$ solid solution with high phase purity. This indicates that $CeO_2$ can completely incorporate the bigger $La^{3+}$ ions, while still retaining its fluorite structure. The fluorite structure of LC powder prepared by solid-state synthesis was also identified at 1300 °C and 1400 °C by Dehkharghani et al. [29] and Zhang et al. [31], respectively.

As expected, the un-calcined LC40Z powder mixture consists of two phases corresponding to the original reagents, namely the fluorite-type LC phase (PDF-01-084-8347) and the YSZ powder with cubic crystallographic structure (c-$ZrO_2$, PDF-04-049-1642), without the formation of any new phase. As for the LC40Z powder mixture calcined at 1300 °C, XRD showed that the compound is also a mixture of LC and c-$ZrO_2$. Moreover, a small fraction of a new phase, namely $La_2Ce_{0.2}Zr_{1.8}O_7$ (LCZ, PDF-04-024-9518) is observed, indicating that the reactions occurred between YSZ and LC during the heat treatment of LC/YSZ powder mixtures. After calcining the LC40Z sample at 1400 °C, there are also mixed phases (LCZ, LC, and c-$ZrO_2$) in the corresponding XRD pattern. However, the intensity of diffraction peaks belonging to LCZ increased when increasing the calcination temperature, while the intensities of the LC and c-$ZrO_2$ peaks gradually decreased. Moreover, the characteristic peak of the pyrochlore structure at 2θ = 36.5° appeared in the XRD pattern, which points to the fact that the newly formed LCZ solid solution is a pyrochlore structure. In the case of LC40Z calcined at 1500 °C, the pyrochlore LCZ turned out to be the dominant phase, and only a low fraction of the initial LC solid solution is observed, with the weak peaks located on the left side of the LCZ phase. Moreover, small peaks belonging to c-$ZrO_2$ still occur on the right side of the LCZ peaks. Furthermore, as shown in Fig. 3, the diffraction peaks of LC in all powder mixtures are shifted to large angles, in contrast to those of pure LC powder. This indicates that the LC in powder mixtures exhibits non-stoichiometric composition. The peaks of c-$ZrO_2$ also showed slight deviation in peak positions; however, the shift was to

lower diffraction angles. This is clearly seen in Fig. 3b, showing that the main c-$ZrO_2$ peak at 2θ = 30° shifted to the left side and almost merged with the LCZ peak with a rising temperature. This indicates that the small amount of La and/ or Ce cations from the original LC lattice interchanged with $Zr^{4+}$ ions in the YSZ lattice [32]. These results are consistent with a study by Liu et al. [37]. The authors observed new pyrochlore diffraction peaks in LC/YSZ compact samples after heat treatment at 1100−1400 °C. It was found that these peaks originated from the reaction between YSZ and LC and the mutual interdiffusion of Ce/La and Zr/Y ions. The strong interaction between LC and YSZ was ascribed to the significant difference in Gibbs free energy, which led to the elemental redistribution and formation of pyrochlore $La_2O_3$−$CeO_2$−$ZrO_2$ solid solution.

The investigation of the LC40Z powder mixtures revealed that the pyrochlore and fluorite structures coexist after calcination in the temperature range of 1300−1500 °C. All LC40Z powder mixtures were heat treated without being pressed into pellets, which may explain the incomplete reaction and the presence of peaks of original reagents (i.e. LC and YSZ) in XRD diffraction patterns (Fig. 3).

XRD patterns of LC40Z bulk samples hot-pressed at different temperatures are shown in Fig. 4. In all samples, the dominant phase is the pyrochlore-type LCZ, confirming that the solid solution reactions between YSZ and LC also occurred during the hot-pressing of LC/YSZ powder mixtures. Besides the main LCZ phase, a very small amount of the initial fluorite LC solid solution is detected in the LC40Z samples sintered at 1300 and 1400 °C. Interestingly, the XRD analysis revealed that no diffraction peaks corresponding to c-$ZrO_2$ were found in either case. This indicates that all $Zr^{4+}$ cations incorporated into the LC lattice with subsequent formation of the LCZ solid solution. Evidently, the complete transition from fluorite to pyrochlore occurred in the LC40Z bulk sample hot-pressed at 1500 °C as the LCZ became the only phase detected in XRD patterns. The absence of residual LC and c-$ZrO_2$ implies that these two materials were completely consumed during the
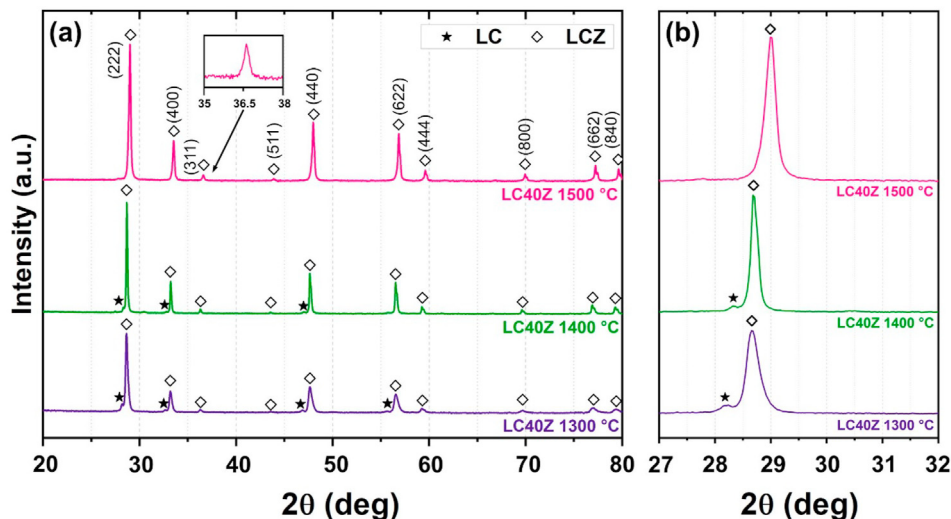
**Fig. 4 − XRD patterns of the hot-pressed LC40Z bulk samples: (a) 2θ range 20−80° (insert in XRD pattern shows a magnification of the LCZ pyrochlore peak at 2θ = 36.5°); (b) 2θ range 27−32°.**

reaction, yielding a more stable substance. A possible explanation for the complete phase transformation in the LC40Z bulk sample is that high sintering temperature together with applied pressure rendered the randomly distributed $La^{3+}$ ions much more active, followed by their rearrangement into the pyrochlore structure with regular ion configuration [38]. Moreover, it is necessary to point out that the LCZ diffraction peaks in the hot-pressed composites became more intense and sharper than those in the powder mixtures calcined at the same temperatures. This is mainly due to the increase in grain size after sintering.

It is also important to note that all LCZ are pyrochlore-type structures. Also, in this case, the formation of pyrochlore structure is proved by the presence of two characteristic peaks at ~36.6° and ~44° of 2θ in XRD patterns of bulk samples, although the intensities of these peaks are significantly lower compared to those of the main peaks. The existence of these two characteristic peaks is always used to distinguish pyrochlore structure from fluorite structure [23]. As can be observed in Fig. 3, the characteristic pyrochlore peaks at ~44° cannot be seen in XRD patterns because of the weaker intensities of LCZ pyrochlore peaks in LC/YSZ powder mixtures compared to the composite bulk samples prepared by hot-pressing.

Fig. 4b shows the XRD patterns of LC40Z bulk samples in the 2θ range of 27−32°. Although the c-$ZrO_2$ peaks vanished, the residual LC phase still remained in samples sintered at 1300 and 1400 °C. A shift in the peak positions of LC and LCZ to a large angle suggests that compositional changes and substitution of cations occurred, mainly the substitution of $Ce^{4+}$ ions ($Ce^{4+}$ = 0.087 nm) by smaller $Zr^{4+}$ (0,072 nm) [31,39]. Finally, upon further raising the sintering temperature to 1500 °C, the LC peaks totally disappeared and no other phases were detected. Therefore, it can be concluded that the formation of LCZ was completed and the pure LCZ phase was obtained. In addition, 2θ values of the LCZ peaks in powder mixtures and bulk samples were almost identical, implying

that the newly formed solid solution had the same or very similar stoichiometric composition.

Several authors investigated chemical reactivity and compatibility between LC and YSZ. Zhang et al. [31] found that a solid solution reaction between YSZ and LC took place during atmospheric plasma spraying to form (La, Y)$_2$(Ce, Zr)$_2$O$_7$ solid solution when YSZ content is in the range of 10−40 mol %. Xu et al. [40] also studied potential interactions between LC and YSZ in LC-YSZ composite coatings after heat treatment at 1300 °C. The authors also reported that a severe reaction between LC and YSZ occurred. However, the reaction products consisted of La$_2$Zr$_2$O$_7$ (LZ) and CeO$_2$. Yi et al. [41] studied the chemical compatibility between La$_2$(Ce$_{1-x}$Zr$_x$)$_2$O$_7$ and YSZ composites at high temperatures (1100−1300 °C). The authors found that the reaction between these two materials generates similar products of La$_2$O$_3$−CeO$_2$−ZrO$_2$ solid solutions with fluorite structure. Moreover, the results revealed that chemical compatibility increased with increasing Zr fraction in La$_2$(Ce$_{1-x}$Zr$_x$)$_2$O$_7$. Similar results have been reported in the work of Zhang et al. [42] who studied the thermal stability and thermophysical properties of plasma-sprayed La$_2$Ce$_{1.7}$Ta$_{0.3}$O$_{7.15}$ (LCT) coatings, which were developed by partial substitution of CeO$_2$ in LC with Ta$_2$O$_5$. Since no diffraction peaks belonging to Ta$_2$O$_5$ were detected in the LCT diffraction patterns, the authors concluded that Ta$^{5+}$ entered the LC lattice, leading to the formation of an LCT solid solution.

The detailed results of XRD analysis are summarized in Table 1, including the calculated lattice parameters and 2θ values of the most intense peaks of pyrochlore LCZ (P, 222) and fluorite LC phase (F, 111) in the XRD patterns of all LC40Z composite materials. In the LC powder, the initial 2θ value of the (111) line is 27.93°, and the lattice parameter is 0.5529 nm. As is evident from Table 1, the 2θ values of both fluorite and pyrochlore phases rose with increasing sintering temperature. No influence of the calcination temperature on the lattice parameters of the LCZ in LC40Z powder mixtures was observed. In contrast, the lattice parameters of LCZ and LC in

**Table 1 – Calculated lattice parameters and 2θ values of the diffraction peaks corresponding to LC and LCZ phases.**

| Temperature (°C) | a of LC (nm) | a of LCZ (nm) | 2θ of F in LC (°) | 2θ of P in LCZ (°) |
|---|---|---|---|---|
| 1300 °C p. | 0.5523 | 1.0686 | 27.96 | 28.92 |
| 1400 °C p. | 0.5501 | 1.0681 | 28.07 | 28.94 |
| 1500 °C p. | 0.5445 | 1.0686 | 28.37 | 28.92 |
| 1300 °C b. | 0.5480 | 1.0788 | 28.18 | 28.64 |
| 1400 °C b. | 0.5454 | 1.0767 | 28.32 | 28.70 |
| 1500 °C b. | – | 1.0654 | – | 29.01 |

*p. – powder mixture, b. – bulk sample.

LC40Z bulk samples decreased with increasing sintering temperature due to the dissolution of the high amount of $Zr^{4+}$ cations with smaller ionic radius [37]. As a result, the lattice volume of LC and LCZ shrank and the lattice parameter decreased in order to attain the lowest system energy. Simultaneously, a certain amount of oxygen vacancies is created in the lattice structure due to the charge compensation mechanism [43]. The shift of diffraction peaks and variation of lattice parameters in bulk samples could also be attributed to the thermal residual stress generated during the cooling process, due to the difference in CTEs between LC and YSZ [41,44].

The relative contents of crystalline phases determined by Rietveld refinement of XRD data in both LC40Z powder mixtures and hot-pressed bulk samples are presented in Fig. 5. As shown in Fig. 5a, there was approximately 33% LC and 54% c-$ZrO_2$ in the powder samples calcined at 1300 °C, while only about 13% LCZ was formed as a result of chemical reactions between LC and YSZ. By increasing the calcination temperature to 1400 °C, the LCZ content increased to 23%. A subsequent raising of the temperature to 1500 °C led to a further increase in the LCZ content to 40%, but 14% LC and 46% c-$ZrO_2$ remained in the powder sample. As for the hot-pressed LC40Z bulk samples, no c-$ZrO_2$ was detected in either case. In the bulk sample sintered at 1300 °C, the content of the initial LC phase was only about 5%, and 95% LCZ was formed. When the sintering temperature was 1400 °C, the LCZ content gradually increased to 98%, while the LC content decreased to 2%.

Finally, after sintering at 1500 °C, the content of LCZ reached 100%. These results indicate that the applied pressure during hot pressing accelerated the reaction and diffusion rate between LC and YSZ, leading to a higher production rate of the phase-pure LCZ solid solution. It has been reported that materials with pyrochlore structure are preferable candidates for TBCs as they exhibit better structural stability while fluorite-type materials are susceptible to phase transformation at high temperatures [45]. Yang et al. [45] investigated the sintering resistance and structural evolution of $La_2(Zr_{0.75}Ce_{0.25})_2O_7$ coating at different temperatures. It was observed that the coating transformed from fluorite to pyrochlore at 900 °C. When the temperature reached or exceeded 1100 °C, the phase transformation was completed and the investigated coating exhibited only a pyrochlore structure.

### 3.4. Raman spectroscopy of the LC40Z powder mixtures and the hot-pressed composites

Raman spectroscopy was used for further analysis of the crystalline structure evolution of the LC40Z samples. This method is also an efficient tool to distinguish the pyrochlore and fluorite structures. Fig. 6 shows Raman spectra of LC40Z powder mixtures and bulk samples sintered at 1300–1500 °C. For comparison, the Raman spectrum of the LC powder produced by solid-state synthesis is also plotted in Fig. 6a.

According to the literature [46–48], the Raman spectra of ordered pyrochlore compounds exhibit six characteristic vibrational peaks in the range of 200–1000 $cm^{-1}$, which are assigned to $A_{1g} + E_g + 4F_{2g}$ modes. Conversely, the disordered fluorite structure has only one allowed Raman active mode $F_{2g}$ around 460 $cm^{-1}$, which represents the vibration of oxygen atoms around each cation [49]. As shown in Fig. 6a, the Raman spectrum of the pure LC powder shows one dominant band at ~455 $cm^{-1}$ ($F_{2g}$), one broader band at ~575 $cm^{-1}$, and four weak bands at lower frequencies. The band at ~575 $cm^{-1}$ is ascribed to oxygen vacancies, which are a consequence of $La^{3+}$ embedding into a fluorite-type $CeO_2$ matrix [23]. The weak bands at low frequencies can be attributed to second-order scattering and forbidden acoustic modes caused by defects in the structure [13,50]. For the uncalcined LC40Z powder mixture, no new Raman peaks were observed. However, in
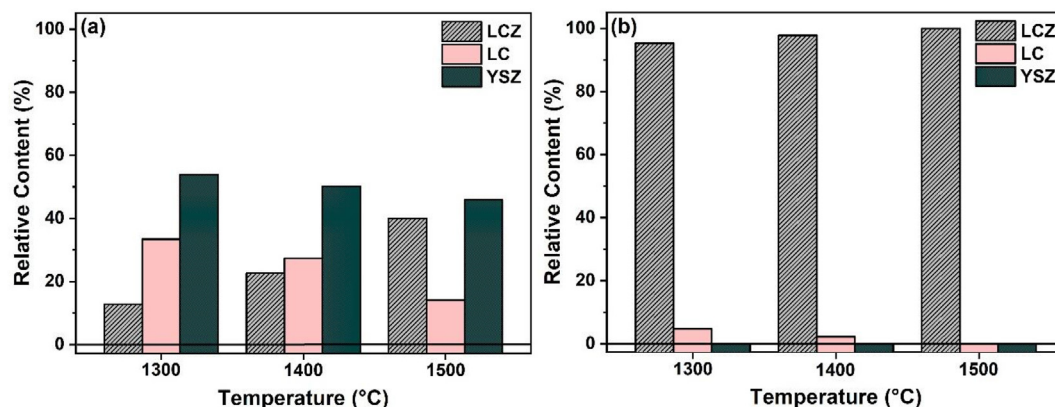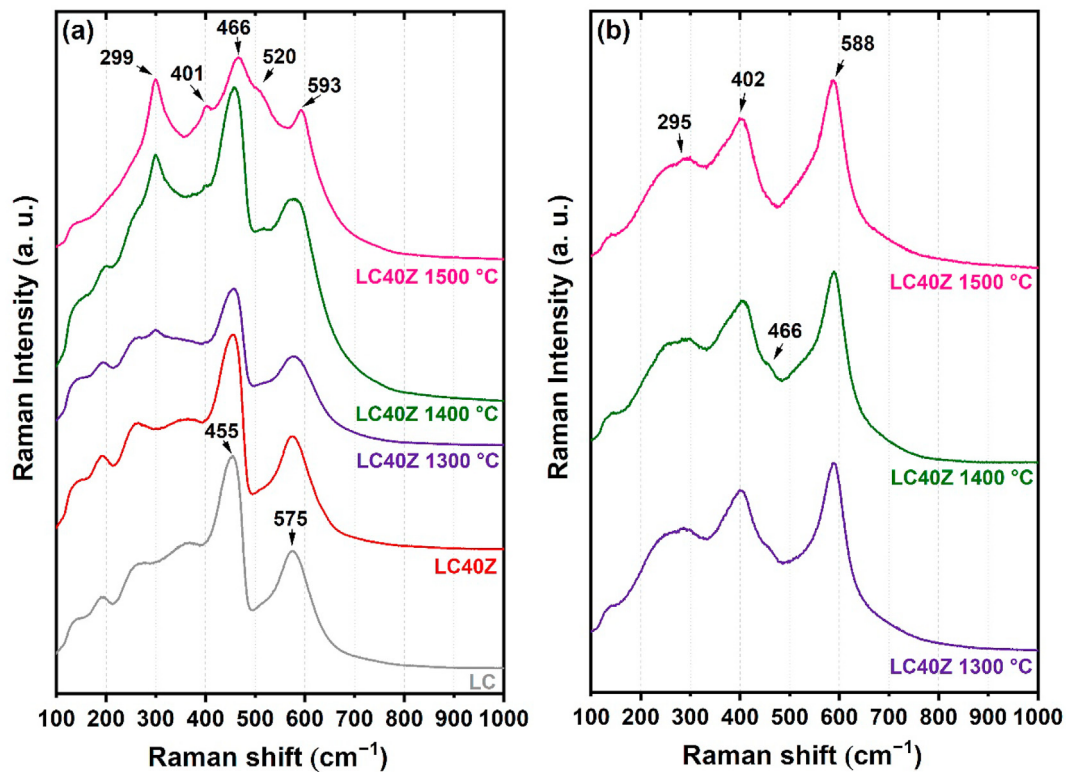


Fig. 5 – Relative contents of crystalline phases determined by the Rietveld refinement of XRD patterns: (a) LC40Z powder mixtures; (b) LC40Z bulk samples.

Fig. 6 – The Raman spectra of (a) LC40Z powder mixtures; (b) LC40Z bulk samples.

addition to the initial fluorite bands, a new Raman band emerged at ~299 cm$^{-1}$ in the LC40Z powder sample after calcination at 1300 °C. After calcining the sample at 1400 °C, the predominance of the pyrochlore phase started to appear, as new pyrochlore peaks at ~401 cm$^{-1}$ and ~520 cm$^{-1}$ became visible in the spectrum. With Zr$^{4+}$ gradually substituting Ce$^{4+}$, the LC undergoes a transition from fluorite to pyrochlore LCZ structure, which was demonstrated by the progressive narrowing of Raman peaks, and the gradual appearance of characteristic pyrochlore bands. The Raman bands at ~460 cm$^{-1}$, representing the fluorite F$_{2g}$ mode, shifted slightly to higher frequencies, indicating bond shortening and strengthening due to element substitution [47].

The Raman spectra of LC40Z bulk samples sintered at 1300−1500 °C are presented in Fig. 6b. The most intense bands are found at ~402 cm$^{-1}$ and ~588 cm$^{-1}$ and correspond to E$_g$ and F$_{2g}$ modes of pyrochlore structure, respectively [51]. In addition, a bulge corresponding to F$_{2g}$ mode was detected in the spectra at ~295 cm$^{-1}$. However, a significant drop in the intensity of this band is observed for bulk samples in contrast to those of the powder mixtures. All other pyrochlore bands became sharp and clear after sintering, suggesting that there were obvious structural changes. As for the LC40Z bulk samples sintered at 1300 and 1400 °C, besides the three typical Raman bands of pyrochlore structure, a fluorite band at ~466 cm$^{-1}$ is also observed, but with very low intensity. With the increase in the sintering temperature to 1500 °C, only typical Raman bands of pyrochlore structure are detected, while the weak fluorite band completely disappeared. The bands at ~588 cm$^{-1}$ exhibit higher intensity for bulk samples compared to powder mixtures, probably due to the formation

of a higher number of oxygen vacancies. Additionally, the peak positions in LC40Z bulk samples are slightly different from those for powder mixtures, because the latter contained a mixture of fluorite and pyrochlore phases. All Raman spectroscopy results strongly correspond with the XRD results discussed in Section 3.3. Our results are also consistent with those reported by Yang et al. [45], who studied La$_2$(Zr$_{0.75}$Ce$_{0.25}$)$_2$O$_7$ as a thermal barrier coating material, and showed that only the pyrochlore phase can be detected in the final bulk ceramics.

### 3.5. Density and microstructures of the hot-pressed composites

The relative densities of the LC40Z bulk samples after sintering are summarized in Table 2. It should be noted that all composites densified by hot-pressing have a high relative density above 95% due to the high temperatures and pressure in the sintering process. The density of the bulk sample hot-pressed at 1500 °C is almost consistent with that of

Table 2 – Relative densities and average grain sizes of the investigated LC40Z bulk samples sintered at different temperatures.

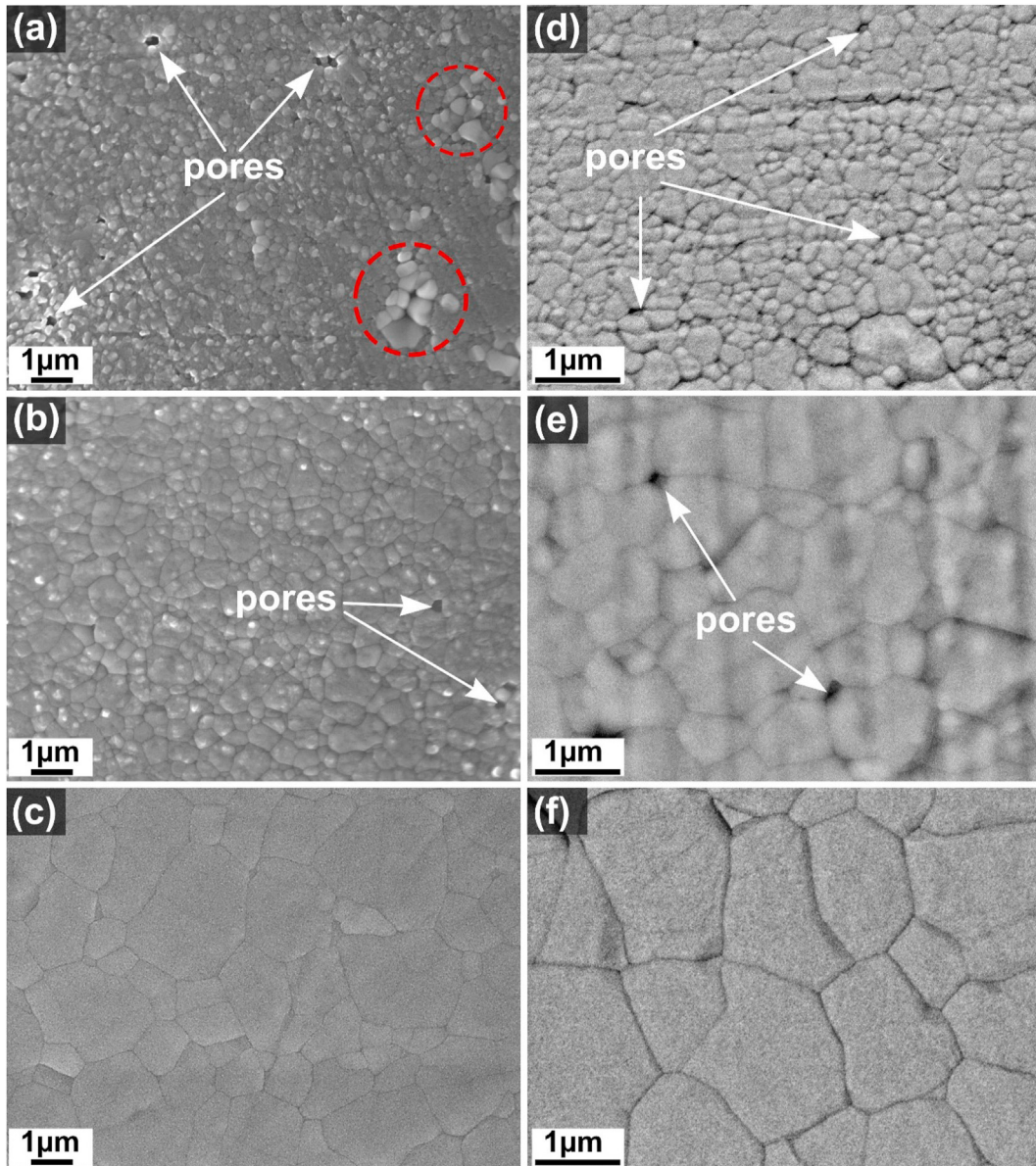| Sintering Temperature (°C) | Relative Density (%) | Average Grain Size (μm) |
| --- | --- | --- |
| 1300 °C | 95.6 | 0.16 ± 0.09 |
| 1400 °C | 97.2 | 0.39 ± 0.21 |
| 1500 °C | 98.9 | 1.02 ± 0.58 |

**Fig. 7 — The SEM microstructures of the thermally etched surfaces of LC40Z bulk samples hot-pressed at different temperatures: (a) 1300 °C; (b) 1400 °C; (c) 1500 °C. High magnification back-scattered SEM images of the thermally etched surfaces of LC40Z bulk samples hot-pressed at different temperatures: (d) 1300 °C; (e) 1400 °C; (f) 1500 °C.**

theoretical density, and the relative density shows a maximum value of 98.9%. As for the LC40Z bulk samples sintered at 1300 and 1400 °C, reduction of density was observed, and the relative densities of those composites are 95.6 and 97.2%, respectively. Wang et al. [52] used cold-pressing at uniaxial pressure of 100 MPa before sintering at 1400 °C for 2 h to obtain $La_2(Zr_{1-x}Ce_x)_2O_7$ ceramics with relative densities >98.8%. Zhou et al. [53] prepared Ce-doped $La_2Zr_2O_7$ ceramics with a relative density of 95.3% using cold-pressing with 100 MPa pressure and pressureless sintering at temperatures up to 1650 °C for 10 h. In our study, hot-pressing conditions were sufficient to obtain relative densities close to the theoretical densities predicted by the mixing law.

SEM micrographs from thermally etched surfaces of LC40Z sintered composites are compared in Fig. 7. The

microstructure of the LC40Z bulk samples hot-pressed at 1300 °C (Fig. 7a) is characterized by the presence of a coarser and elongated matrix composed of grains that can be considered to be LCZ based on XRD analysis. Moreover, randomly distributed regions of aggregations of sub-micron particles (highlighted by red circles in Fig. 7a) are found in the matrix. These grains are around 0.5—1 μm in size and are much bigger than those of the LCZ matrix. This indicates that the morphology of the original LC40Z powder was preserved after hot-pressing at 1300 °C, and a small fraction of the powder experienced no sintering. This is in agreement with the XRD results shown in Fig. 4. Furthermore, pores with random shapes and sizes up to 0.5 μm were detected in the bulk samples prepared by hot-pressing at 1300 °C, and most of the pores were surrounded by un-sintered particles. As can be
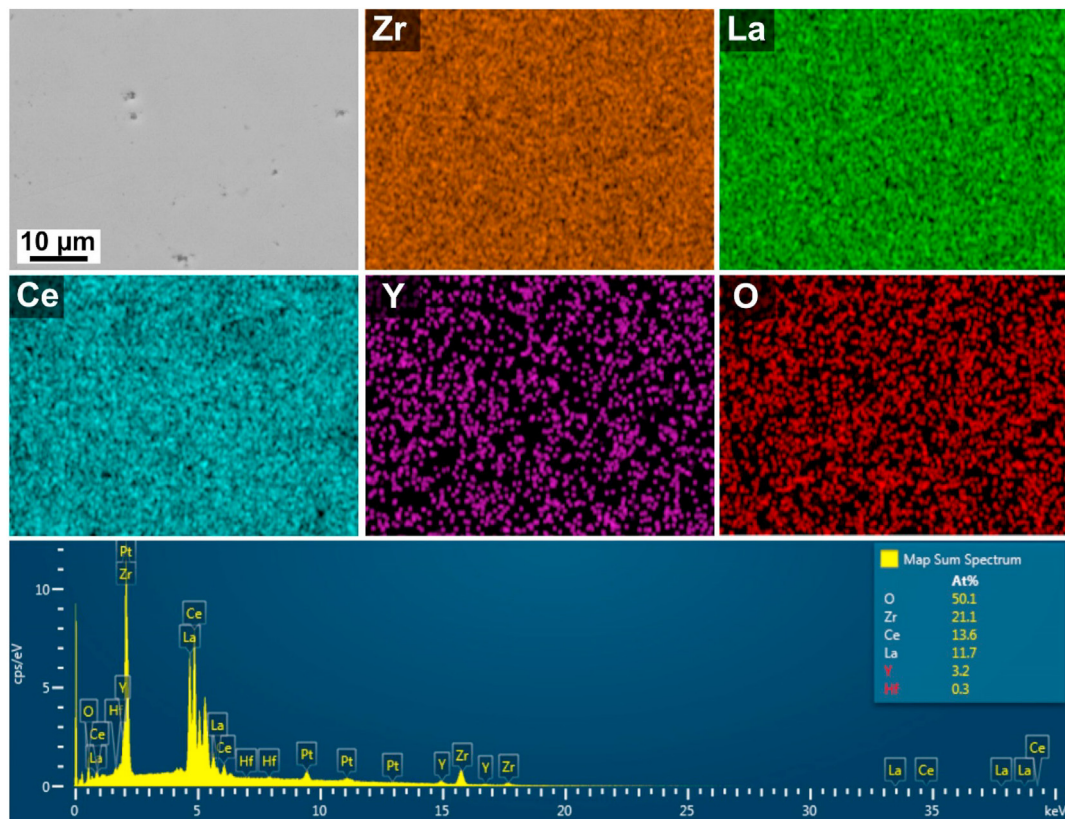
**Fig. 8 — EDXS elemental mapping of the polished surface of LC40Z bulk sample sintered at 1400 °C.**

seen in Fig. 7b, the microstructure of the LC40Z bulk sample hot-pressed at 1400 °C is different from that of the bulk sample sintered at 1300 °C. The aggregation of the originally obtained LC40Z powders almost disappeared, and the sintering degree was more intense. The interfaces and grain boundaries were clearly observed, while only a small number of pores were present in the matrix. However, the pores were getting smaller, indicating that densification occurred. Furthermore, the average grain size significantly increased because of the higher sintering temperature employed during hot-pressing. For the LC40Z bulk samples hot-pressed at 1500 °C (Fig. 7c), the sizes of grains are largest among the studied samples. The LCZ grains are connected directly at the interfaces, while no unreacted phases exist in boundaries between the individual grains. Notably, there are no obvious pores in the grain boundaries or other regions of the etched surface, indicating almost complete densification of the sample. As can be seen from the magnified back-scattered SEM images (Fig. 7d—f), the absence of microstructural differences confirms the homogeneous distribution of the LCZ grains in the composite matrices. EDXS elemental map of the LC40Z sample sintered at 1400 °C, shown in Fig. 8 as the representative, further supports these findings. The distribution of elements (La, Ce, Zr, Y and O) in the composite is highly homogeneous without a significant contrast difference. This confirms the formation of LCZ solid solutions, which is consistent with the phase evaluation results by XRD. It has been reported that YSZ and LC-based materials have low sintering resistance above 1280 °C, which is related to the rapid shrinkage of materials and sealing of the pores [14]. However, Liu et al. [37] found that

with increasing sintering temperature, both the number and size of pores in LC-YSZ composites increased dramatically, indicating improved sintering resistance of the specimens.

The resulting average grain size of LC40Z composites evaluated from SEM micrographs are presented in Table 2. The average grain size in the LC40Z sample hot-pressed at 1300 °C is 0.16 ± 0.09 μm, while the average grain size increased to 1.02 ± 0.58 μm for the sample sintered at 1500 °C. In contrast, both porosity and pore size decreased with increasing sintering temperature, which corresponds well with the results of the relative densities of the bulk samples shown in Table 2.

Sintering of bulk materials is typically described as the removal of intergranular pores caused by lattice and grain boundary diffusion at high temperatures [38]. Grain growth in composite materials with high chemical compatibility is usually inhibited by the introduction of a secondary phase due to a significant "pinning" effect between grains of different phases. In other words, the average grain size of the matrix decreases as the volume fraction of the secondary phase increases [41,54]. However, in our previous work [32], the grain coarsening and grain growth were observed with the increasing wt. fraction of YSZ in the hot-pressed LC-YSZ bulk samples. Furthermore, both large and small grains were detected in the composites containing 60 wt% and 70 wt% of YSZ, which was attributed to the higher content of YSZ and subsequent consumption of small LCZ grains during sintering. Liu et al. [37] also reported a rapid grain growth in LC-YSZ composites, which was ascribed to the high activation energy of nanosized crystals and high diffusion rates of $Ce^{4+}$ and
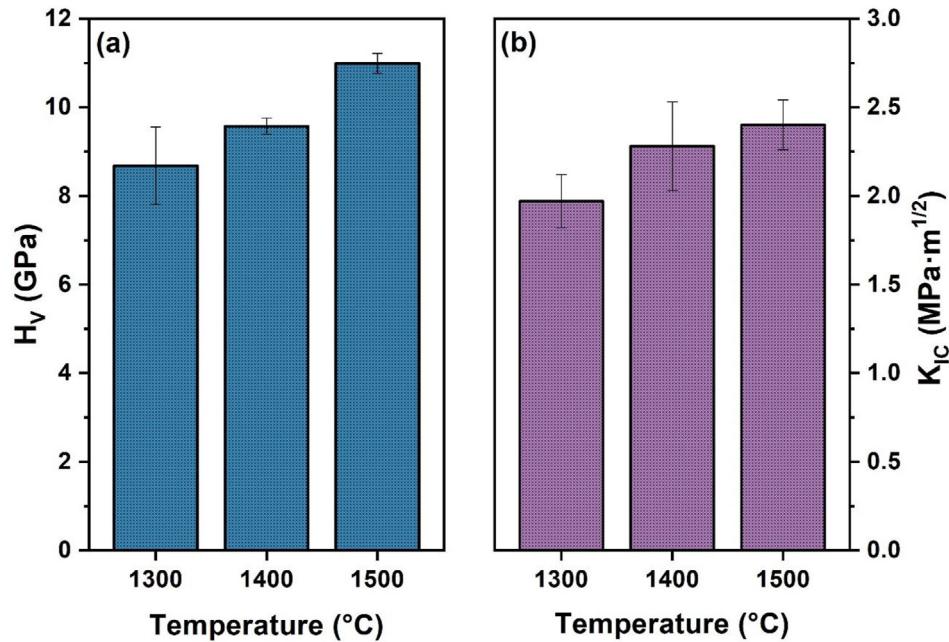
**Fig. 9** — **The mechanical properties of LC40Z ceramic composites hot-pressed at different temperatures: (a) Vickers hardness; (b) fracture toughness.**

La$^{3+}$ cations. Therefore, the authors assume that the grain growth mechanism originated from grain boundary migration. Consequently, tiny grains were consumed during the sintering process. In the present work, we conclude that the reaction effect and interdiffusion between LC and YSZ particles also contributed to the grain growth in the hot-pressed LC/YSZ samples.

### 3.6. Mechanical properties of the hot-pressed composites

The mechanical properties represent the critical factors in determining the durability of TBCs. Generally, high hardness and high fracture toughness are desirable for TBC materials to sustain a satisfying service life. Microhardness serves as a crucial indicator for assessing the resistance of materials to deformation, scratching, and erosion. The Vickers hardness (H$_V$) values of the LC40Z composites, hot-pressed at different temperatures are presented in Fig. 9a. At least 10 valid indentations were made under a given load of 5 N, and the average value was identified as the hardness of the composite bulk samples. Experimental results showed that the H$_V$ of LC40Z composites increased gradually with an increasing sintering temperature. The H$_V$ for LC40Z bulk sample sintered at 1300 °C is 8.68 ± 0.87 GPa, while the H$_V$ of the bulk sample sintered at 1400 °C was improved to 9.57 ± 0.18 GPa. The highest hardness value of 10.99 ± 0.23 GPa was obtained for the composite material hot-pressed at 1500 °C.

Two of the main aspects influencing the mechanical properties of ceramic composites are their composition and microstructure features. More specifically, the increase in grain size and almost complete densification, which was reflected in the high relative density, are the main factors that enhanced the H$_V$ of the LC40Z sample sintered at 1500 °C. In general, the hardness of ceramic composites inversely

correlates with the porosity level. A considerably lower residual porosity in the LC40Z bulk sample sintered at 1500 °C resulted in a denser microstructure, and thus higher H$_V$ compared to the bulk sample sintered at 1300 °C. Moreover, as mentioned in Section 3.3, the high amount of Zr$^{4+}$ cations dissolved in the LC lattice during hot-pressing, which led to crystal cell shrinking and lattice distortion. The lattice distortion can improve materials' ability to resist deformation and thereby increase the hardness [31].

In addition to the Vickers hardness, the fracture toughness (K$_{IC}$) of the LC40Z bulk samples hot-pressed at different temperatures was determined from the corresponding indentation images. The fracture toughness of ceramic materials provides an indication of their ability to resist crack propagation. The higher the value of fracture toughness, the more difficult the material is to break. Therefore, the high fracture toughness is beneficial for the durability of TBCs under thermomechanical loading. The K$_{IC}$ values of the LC40Z bulks are visualized in Fig. 9b.

The K$_{IC}$ results showed the same dependence on the sintering temperature as in the case of Vickers hardness tests. The K$_{IC}$ of the LC40Z composites improved with increasing sintering temperature and the maximum K$_{IC}$ of 2.40 ± 0.14 MPa m$^{1/2}$ was achieved for the bulk sample hot-pressed at 1500 °C. For all LC40Z specimens, the surface indentation patterns (Fig. 10) exhibited radial cracks at four indent corners, and the cracks were relatively short and did not indicate buckling. It is assumed that the increased fracture toughness of the LC40Z ceramic composites can be attributed to the reaction of LC and YSZ and the subsequent coarser-grained microstructure. According to Zhang et al. [31], the incorporation of YSZ into the LC lattice could enhance the lattice's cohesive energy, which is proportional to the fracture energy. Therefore, the improved fracture toughness of YSZ-
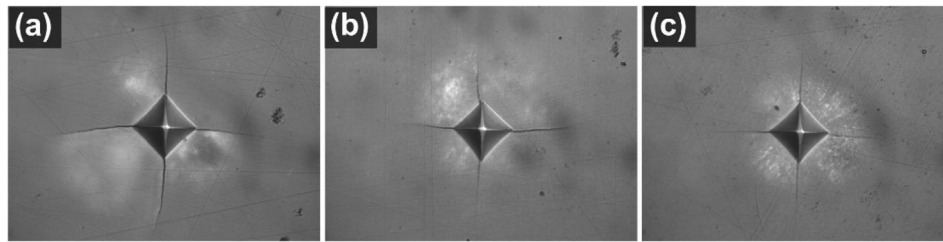
**Fig. 10 — Vickers indentation patterns of the LC40Z ceramic composites hot-pressed at different temperatures: (a) 1300 °C; (b) 1400 °C; (c) 1500 °C.**

reinforced LC composite TBCs was thought to be due to the increased fracture energy resulting from the solid-solution reaction between YSZ and LC.

Due to its relatively high fracture toughness compared to other TBC candidates, YSZ is commonly used to improve the fracture toughness of rare-earth element based-ceramics, partially due to its phase transformation toughening mechanism [31,55,56]. The fracture toughness of the LC40Z composite bulk samples investigated in this work was found to be higher than that of 8YSZ (~2 MPa m$^{1/2}$) [4], but lower than that of bulk $La_2(Zr_{1-x}Ce_x)_2O_7$ ceramics (3.5—3.8 MPa m$^{1/2}$) [57]. In the published report of Kang et al. [[58]], the fracture toughness of LC/50 vol% YSZ composite TBC coating was reported as 1.48 ± 0.26 MPa m$^{1/2}$, which is higher than that of single LC coating (0.72 ± 0.15 MPa m$^{1/2}$). The improved fracture toughness of plasma-sprayed LC/8YSZ coating was also reported by Liu et al. [59]. The $K_{IC}$ of the LC/8YSZ interface was 1.17 ± 0.24 MPa m$^{1/2}$, which was larger than the LC (0.41 ± 0.15 MPa m$^{1/2}$). YSZ was also used for fracture toughness improvement of $Gd_2Zr_2O_7$ ceramics by Zhang et al. [39], and $La_2Zr_2O_7$ ceramics as reported by Wang et al. [55] and Zhang et al. [60].

## 4. Conclusions

In this work, hot-pressed LC40Z composites with high relative densities were prepared and studied as a material designed for TBC applications. The chemical reactivity between LC and YSZ, phase composition, microstructure evolution, and mechanical properties of the composites were studied in detail as a function of sintering temperatures. The main conclusions are summarized as follows.

(1) XRD data analysis revealed that the hot-pressing process produces a reaction between LC and YSZ since a new pyrochlore LCZ phase was detected. The fraction of the LCZ was found to increase with increasing sintering temperature, while no initial LC and cubic phase of YSZ was found to exist in bulk sample sintered at 1500 °C. This indicates that $Zr^{4+}$ gradually substituted $Ce^{4+}$ in the LC lattice with a subsequent transition of fluorite LC to pyrochlore LCZ structure, which was also confirmed by Raman spectroscopy.

(2) All prepared composites exhibited high relative density above 95%. SEM analysis confirmed that densification occurred and the grain size grew while porosity decreased when raising the sintering temperature. The average grain size significantly increased from 0.16 ± 0.09 μm to 1.02 ± 0.58 μm after sintering at 1500 °C.

(3) The Vickers hardness values increased gradually with increasing sintering temperature due to the denser microstructure with homogeneous grains and reduced porosity. The fracture toughness results showed the same dependence on sintering temperature. The Vickers hardness of LC40Z composites ranged from 8.68 ± 0.87 GPa to 10.99 ± 0.23 GPa, and the fracture toughness ranged from 1.97 ± 0.15 to 2.4 ± 0.14 MPa m$^{1/2}$.

(4) Comparing all the results together with mechanical property measurements, it can be concluded that the optimal sintering temperature for hot-pressed LC40Z composites is 1500 °C. The findings of this study provide important information for the design of a desirable, high-performing TBC system.

## Declaration of competing interest

The authors declare that they have no known competing financial interests or personal relationships that could have appeared to influence the work reported in this paper.

## Acknowledgement

REFERENCES

[1] Pakseresht AH, Rahimipour MR, Alizadeh M, Hadavi SMM, Shahbazkhan A. Concept of advanced thermal barrier functional coatings in high temperature engineering

components. Res. Perspect. Funct. Micro- Nanoscale Coatings 2016:396–419. https://doi.org/10.4018/978-1-5225-0066-7.ch015.

[2] Mauer G, Jarligo MO, Mack DE, Vaßen R. Plasma-sprayed thermal barrier coatings: new materials, processing issues, and solutions. 2013 225 J Therm Spray Technol 2013;22:646–58. https://doi.org/10.1007/S11666-013-9889-8.

[3] Cao XQ, Vassen R, Jungen W, Schwartz S, Tietz F, Stöver D. Thermal stability of lanthanum zirconate plasma-sprayed coating. J Am Ceram Soc 2001;84:2086–90. https://doi.org/10.1111/J.1151-2916.2001.TB00962.X.

[4] Vassen R, Cao X, Tietz F, Basu D, Sto D. Zirconates as new materials for thermal barrier coatings. J Am Ceram Soc 2000;83:2023–8. https://doi.org/10.1111/j.1151-2916.2000.tb01506.x.

[5] Schlichting KW, Padture NP, Klemens PG. Thermal conductivity of dense and porous yttria-stabilized zirconia. J Mater Sci 2001;36:3003–10. https://doi.org/10.1023/A:1017970924312.

[6] Pakseresht A, Sharifianjazi F, Esmaeilkhanian A, Bazli L, Reisi Nafchi M, Bazli M, et al. Failure mechanisms and structure tailoring of YSZ and new candidates for thermal barrier coatings: a systematic review. Mater Des 2022;222:111044. https://doi.org/10.1016/j.matdes.2022.111044.

[7] Brandon JR, Taylor R. Phase stability of zirconia-based thermal barrier coatings part II. Zirconia-ceria alloys. Surf Coating Technol 1991;46:91–101. https://doi.org/10.1016/0257-8972(91)90152-M.

[8] Zhang J, Guo X, Jung Y-G, Li L, Knapp J. Lanthanum zirconate based thermal barrier coatings: a review. Surf Coating Technol 2017;323:18–29. https://doi.org/10.1016/j.surfcoat.2016.10.019.

[9] Cao XQ, Vassen R, Stoever D. Ceramic materials for thermal barrier coatings. J Eur Ceram Soc 2004;24:1–10. https://doi.org/10.1016/S0955-2219(03)00129-8.

[10] Alebrahim M, Pakseresht A, Jafari R, Galusek D, Sharifian Jazi F. The effect of additional ceramic fiber on wear and mechanical properties of thermal barrier coatings. Handb. Res. Tribol. Coatings Surf. Treat., IGI Global 2022:1–19. https://doi.org/10.4018/978-1-7998-9683-8.CH001.

[11] Xiang J, Chen S, Huang J, Zhang H, Zhao X. Phase structure and thermophysical properties of co-doped $La_2Zr_2O_7$ ceramics for thermal barrier coatings. Ceram Int 2012;38:3607–12. https://doi.org/10.1016/j.ceramint.2011.12.077.

[12] Hongsong Z, Zhengying W, Yongde Z, Gang L, Zhenjun L. Preparation, characterization of $A_2Ce_2O_7$ (A = La and Gd) and their photo-catalytic properties. Energy Environ Focus 2015;4:324–9. https://doi.org/10.1166/eef.2015.1177.

[13] Zhang FX, Tracy CL, Lang M, Ewing RC. Stability of fluorite-type $La_2Ce_2O_7$ under extreme conditions. J Alloys Compd 2016;674:168–73. https://doi.org/10.1016/j.jallcom.2016.03.002.

[14] Cao X, Vassen R, Fischer W, Tietz F, Jungen W, Stöver D. Lanthanum-cerium oxide as a thermal barrier-coating material for high-temperature applications. Adv Mater 2003;15:1438–42. https://doi.org/10.1002/adma.200304132.

[15] Ma W, Gong S, Xu H, Cao X. The thermal cycling behavior of Lanthanum–Cerium Oxide thermal barrier coating prepared by EB–PVD. Surf Coating Technol 2006;200:5113–8. https://doi.org/10.1016/j.surfcoat.2005.05.033.

[16] Gao L, Guo H, Gong S, Xu H. Plasma-sprayed $La_2Ce_2O_7$ thermal barrier coatings against calcium-magnesium-alumina-silicate penetration. J Eur Ceram Soc 2014;34:2553–61. https://doi.org/10.1016/j.jeurceramsoc.2014.02.031.

[17] Ma W, Gong S, Xu H, Cao X. On improving the phase stability and thermal expansion coefficients of lanthanum cerium oxide solid solutions. Scripta Mater 2006;54:1505–8. https://doi.org/10.1016/j.scriptamat.2005.12.043.

[18] Guo H, Wang Y, Wang L, Gong S. Thermo-physical properties and thermal shock resistance of segmented $La_2Ce_2O_7$/YSZ thermal barrier coatings. J Therm Spray Technol 2009;18:665–71. https://doi.org/10.1007/s11666-009-9350-1.

[19] Fathi Dehkharghani AM, Rahimipour MR, Zakeri M. Crystal structure and lattice parameter investigation of $La^{3+}$ substituted $CeO_2$ in $LaxCe_{1-x}O_{2-X/2}$ synthesized by solid-state method. Adv Ceram Prog 2020;6:43–8. https://doi.org/10.30501/ACP.2020.106445.

[20] Tinwala H, Shah DV, Menghani J, Pati R. Synthesis of $La_2Ce_2O_7$ nanoparticles by co-precipitation method and its characterization. J Nanosci Nanotechnol 2014;14:6072–6. https://doi.org/10.1166/jnn.2014.8834.

[21] Besikiotis V, Knee CS, Ahmed I, Haugsrud R, Norby T. Crystal structure, hydration and ionic conductivity of the inherently oxygen-deficient $La_2Ce_2O_7$. Solid State Ionics 2012;228:1–7. https://doi.org/10.1016/j.ssi.2012.08.023.

[22] Khademinia S, Behzad M. Lanthanum cerate ($La_2Ce_2O_7$): hydrothermal synthesis, characterization and optical properties. Int Nano Lett 2015;5:101–7. https://doi.org/10.1007/s40089-015-0143-x.

[23] Wang Y, Wang C, Li C, Cheng Y, Chi F. Influence of different surfactants on crystal growth behavior and sinterability of $La_2Ce_2O_7$ solid solution. Ceram Int 2014;40:4305–10. https://doi.org/10.1016/j.ceramint.2013.08.096.

[24] Weng SF, Wang YH, Lee CS. Autothermal steam reforming of ethanol over $La_2Ce_{2-x}Ru_xO_7$ (x=0-0.35) catalyst for hydrogen production. Appl Catal B Environ 2013;134–135:359–66. https://doi.org/10.1016/j.apcatb.2013.01.025.

[25] Wang XY, Zhu YP, Zhang WG. Preparation of $La_2Ce_2O_7$ nano-powders by molten salts method. Adv Mater Res 2009;79–82:337–40. https://doi.org/10.4028/www.scientific.net/AMR.79-82.337.

[26] Zhao C, He W, He J, Wei L, Guo H. Correlation of feedstock powder characteristics with microstructure, composition, and mechanical properties of $La_2Ce_2O_7$ coatings produced by plasma spray-physical vapor deposition. Coatings 2020;10:93. https://doi.org/10.3390/coatings10020093.

[27] Wang Y, Guo H, Gong S. Thermal shock resistance and mechanical properties of $La_2Ce_2O_7$ thermal barrier coatings with segmented structure. Ceram Int 2009;35:2639–44. https://doi.org/10.1016/j.ceramint.2009.02.025.

[28] Dong H, Wang D, Pei Y, Li H, Li P, Ma W. Optimization and thermal cycling behavior of $La_2Ce_2O_7$ thermal barrier coatings. Ceram Int 2013;39:1863–70. https://doi.org/10.1016/J.CERAMINT.2012.08.034.

[29] Dehkharghani AMF, Rahimipour MR, Zakeri M. Improving the thermal shock resistance and fracture toughness of synthesized $La_2Ce_2O_7$ thermal barrier coatings through formation of $La_2Ce_2O_7$/YSZ composite coating via air plasma spraying. Surf Coating Technol 2020;399:126174. https://doi.org/10.1016/j.surfcoat.2020.126174.

[30] Ma W, Gong S, Li H, Xu H. Novel thermal barrier coatings based on $La_2Ce_2O_7$/8YSZ double-ceramic-layer systems deposited by electron beam physical vapor deposition. Surf Coating Technol 2008;202:2704–8. https://doi.org/10.1016/j.surfcoat.2007.09.047.

[31] Zhang H, Yuan J, Song W, Zhou X, Dong S, Duo S, et al. Composition, mechanical properties and thermal cycling performance of YSZ toughened $La_2Ce_2O_7$ composite thermal barrier coatings. Ceram Int 2020;46:6641–51. https://doi.org/10.1016/j.ceramint.2019.11.152.

[32] Parchovianský M, Parchovianská I, Hanzel O, Netriová Z, Pakseresht A. Phase evaluation, mechanical properties and thermal behavior of hot-pressed LC-YSZ composites for TBC

applications. Materials 2022;15:2839. https://doi.org/10.3390/ma15082839.

[33] Parchovianská I, Parchovianský M, Pecušová B, Hanzel O, Pakseresht A. Synthesis and characterization of fluorite-type $La_2Ce_2O_7$ plasma sprayable powder for TBCs application. Materials 2022;15:4007. https://doi.org/10.3390/ma15114007.

[34] Shetty DK, Wright IG, Mincer PN, Clauer AH. Indentation fracture of WC-Co cermets. J Mater Sci 1985 205 1985;20:1873—82. https://doi.org/10.1007/BF00555296.

[35] Joulia A, Vardelle M, Rossignol S. Synthesis and thermal stability of $Re_2Zr_2O_7$, ($Re=$La, Gd) and $La_2(Zr_{1-x}Ce_x)_2O_7-\delta$ compounds under reducing and oxidant atmospheres for thermal barrier coatings. J Eur Ceram Soc 2013;33:2633—44. https://doi.org/10.1016/j.jeurceramsoc.2013.03.030.

[36] Horlait D, Claparède L, Clavier N, Szenknect S, Dacheux N, Ravaux J, et al. Stability and structural evolution of $Ce^{IV}_{1-x}Ln^{III}_xO_{2-x/2}$ solid solutions: a coupled μ-Raman/XRD approach. Inorg Chem 2011;50:7150—61. https://doi.org/10.1021/IC200751M/SUPPL_FILE/IC200751M_SI_001.PDF.

[37] Liu XY, Yi H, Che JW, Liang GY. Phase, compositional, structural, and chemical stability of $La_2Ce_2O_7$ after high temperature heat treatment. Ceram Int 2019;45:5030—5. https://doi.org/10.1016/j.ceramint.2018.11.204.

[38] Yi H, Che J, Xu Z, Liang G, Liu X. Sintering resistance of $La_2Ce_2O_7$, $La_2Zr_2O_7$, and yttria stabilized zirconia ceramics. Ceram Int 2021;47:4197—205. https://doi.org/10.1016/j.ceramint.2020.09.298.

[39] Zhang H, Wang J, Dong S, Yuan J, Zhou X, Duo S, et al. Mechanical properties and thermal cycling behavior of $Ta_2O_5$ doped $La_2Ce_2O_7$ thermal barrier coatings prepared by atmospheric plasma spraying. J Alloys Compd 2019;785:1068—76. https://doi.org/10.1016/j.jallcom.2019.01.259.

[40] Xu YX, Liu T, Yang GJ, Li CJ. Thermal stability of plasma-sprayed $La_2Ce_2O_7$/YSZ composite coating. Ceram Int 2016;42:7950—61. https://doi.org/10.1016/j.ceramint.2016.01.179.

[41] Yi H, Liu X, Che J, Liang G. Thermochemical compatibility between $La_2(Ce_{1-x}Zr_x)_2O_7$ and 4 mol% $Y_2O_3$ stabilized zirconia after high temperature heat treatment. Ceram Int 2020;46:4142—7. https://doi.org/10.1016/j.ceramint.2019.10.130.

[42] Zhang H, Sun J, Duo S, Zhou X, Yuan J, Dong S, et al. Thermal and mechanical properties of $Ta_2O_5$ doped $La_2Ce_2O_7$ thermal barrier coatings prepared by atmospheric plasma spraying. J Eur Ceram Soc 2019;39:2379—88. https://doi.org/10.1016/j.jeurceramsoc.2019.02.041.

[43] Liu Y, Bai Y, Li E, Qi Y, Liu C, Dong H, et al. Preparation and characterization of $SrZrO_3$—$La_2Ce_2O_7$ composite ceramics as a thermal barrier coating material. Mater Chem Phys 2020;247:122904. https://doi.org/10.1016/j.matchemphys.2020.122904.

[44] Liu XY, Xu ZH, Liang GY. Comparative study of the sintering behaviors between YSZ and LZ/YSZ composite. Mater Lett 2017;191:108—11. https://doi.org/10.1016/j.matlet.2016.12.105.

[45] Yang P, An Y, Zhao D, Li Y, Zhou H, Chen J. Structure evolution, thermal properties and sintering resistance of promising thermal barrier coating material $La_2(Zr_{0.75}Ce_{0.25})_2O_7$. Ceram Int 2020;46:20652—63. https://doi.org/10.1016/j.ceramint.2020.04.111.

[46] Garcia MAP, Gupta SK, Mao Y. Achieving blue emission via f→d transition from pyrochlore $Eu^{2+}$ and $Ce^{3+}$-doped

$La_2Zr_2O_7$ nanoparticles. J Mol Struct 2020;1220:128688. https://doi.org/10.1016/j.molstruc.2020.128688.

[47] Wang S, Li W, Wang S, Chen Z. Synthesis of nanostructured $La_2Zr_2O_7$ by a non-alkoxide sol—gel method: from gel to crystalline powders. J Eur Ceram Soc 2015;35:105—12. https://doi.org/10.1016/j.jeurceramsoc.2014.08.032.

[48] Wan C, Qu Z, Du A, Pan W. Order-disorder transition and unconventional thermal conductivities of the $(Sm_{1-x}Yb_x)_2Zr_2O_7$ series. J Am Ceram Soc 2011;94:592—6. https://doi.org/10.1111/j.1551-2916.2010.04113.x.

[49] McBride JR, Hass KC, Poindexter BD, Weber WH. Raman and x-ray studies of $Ce_{1-x}RE_xO_{2-y}$, where RE=La, Pr, Nd, Eu, Gd, and Tb. J Appl Phys 1994;76:2435—41. https://doi.org/10.1063/1.357593.

[50] Weber WH, Hass KC, McBride JR. Raman study of $CeO_2$: second-order scattering, lattice dynamics, and particle-size effects. Phys Rev B 1993;48:178—85. https://doi.org/10.1103/PhysRevB.48.178.

[51] Yang P, Bu Z, An Y, Zhou H, Li Y, Chen J. A systematic study on $Na_2SO_4$-induced hot corrosion behavior of plasma-sprayed $La_2(Zr_{0.75}Ce_{0.25})_2O_7$ coating. Surf Coating Technol 2022;429:127979. https://doi.org/10.1016/j.surfcoat.2021.127979.

[52] Wang Y, Yang F, Xiao P. Role and determining factor of substitutional defects on thermal conductivity: a study of $La_2(Zr_{1-x}Bx)_2O_7$ (B=Hf, Ce, 0⩽x⩽0.5) pyrochlore solid solutions. Acta Mater 2014;68:106—15. https://doi.org/10.1016/j.actamat.2014.01.011.

[53] Zhou H, Yi D, Yu Z, Xiao L. Preparation and thermophysical properties of $CeO_2$ doped $La_2Zr_2O_7$ ceramic for thermal barrier coatings. J Alloys Compd 2007;438:217—21. https://doi.org/10.1016/j.jallcom.2006.08.005.

[54] Parchovianský M, Galusek D, Sedláček J, Švančárek P, Kašiarová M, Dusza J, et al. Microstructure and mechanical properties of hot pressed $Al_2O_3$/SiC nanocomposites. J Eur Ceram Soc 2013;33:2291—8. https://doi.org/10.1016/j.jeurceramsoc.2013.01.024.

[55] Wang Y, Xiao P. The phase stability and toughening effect of 3Y-TZP dispersed in the lanthanum zirconate ceramics. Mater Sci Eng, A 2014;604:34—9. https://doi.org/10.1016/j.msea.2014.03.010.

[56] Mercer C, Williams JR, Clarke DR, Evans AG. On a ferroelastic mechanism governing the toughness of metastable tetragonal-prime (t) yttria-stabilized zirconia. Proc R Soc A Math Phys Eng Sci 2007;463:1393—408. https://doi.org/10.1098/RSPA.2007.1829.

[57] Ma W, Li X, Yin Y, Dong H, Bai Y, Liu J, et al. The mechanical and thermophysical properties of $La_2(Zr_{1-x}Ce_x)_2O_7$ ceramics. J Alloys Compd 2016;660:85—92. https://doi.org/10.1016/j.jallcom.2015.11.092.

[58] Kang YX, Bai Y, Fan W, Yuan T, Gao Y, Bao CG, et al. Thermal cycling performance of $La_2Ce_2O_7$/50 vol.% YSZ composite thermal barrier coating with CMAS corrosion. J Eur Ceram Soc 2018;38:2851—62. https://doi.org/10.1016/j.jeurceramsoc.2018.02.025.

[59] Liu K, Bai Y, Li J, Ma J, Du J, Cao Y, et al. Structure-property relationship and design of plasma-sprayed $La_2Ce_2O_7$/8YSZ composite coatings for gas turbine blades. Ceram Int 2018;44:13662—73. https://doi.org/10.1016/j.ceramint.2018.04.204.

[60] Zhang D, Liao K, Yu Y, Tian Z, Cao Y. Microstructure and thermal & mechanical properties of $La_2Zr_2O_7$@YSZ composite ceramic. Ceram Int 2020;46:4737—47. https://doi.org/10.1016/j.ceramint.2019.10.205.